



Supplementary Materials for  
**Optical polarization–based seismic and water wave sensing  
on transoceanic cables**

Zhongwen Zhan\*, Mattia Cantono, Valey Kamalov, Antonio Mecozzi,  
Rafael Müller, Shuang Yin, Jorge C. Castellanos

\*Corresponding author. Email: zwzhan@caltech.edu

Published 26 February 2021, *Science* **371**, 931 (2021)  
DOI: 10.1126/science.abe6648

**This PDF file includes:**

Supplementary Text  
Figs. S1 to S12  
References

## Supplementary Text

### Cable Deployment and Parameters

The Curie cable construction included a 1,300-m bored conduit at the Los Angeles landing, which was followed by 200 km of cable burial when the water depth is shallower than 1000 m. Then cable was laid on the seabed. The water depth along cable Curie is mostly between 3,000 and 5,000 meters. Total length of the Curie cable is 10,429 km. Submarine repeaters with EDFA amplifiers boost the optical power by up to 20 dBm in each fiber every 100 km. The optical D+ fiber (ITU-T G.654) used in the Curie cable has an effective cross-section area of  $130 \mu\text{m}^2$  and a loss of 0.156 dB/km. The PMD (polarization mode dispersion) coefficients of the cabled fibers are in the 0.01 - 0.07 ps/ $\sqrt{\text{km}}$  range. On the Los Angeles end, transmitters and receivers are placed in a data center that connects to the beach manhole through 7 km of buried terrestrial cable. On the Valparaiso end (Fig. S1C), the distance from the beach manhole, where the wet portion was terminated, to the cable landing station through an 0.7 km underground conduit.

### Physics of mechanical perturbations to SOP

An ideal optical fiber is circular and the silica glass of which it is made is isotropic. In the weakly guiding approximation, it supports the propagation of two degenerate orthogonal polarization modes. This means that any couple of orthogonal polarization modes propagates in the fiber with the same wave-vector and, consequently, the polarization is preserved.

In reality, imperfections during construction, stress and other perturbing effects break the cylindrical symmetry of the fiber and make the fiber birefringent. This means that, in a fiber section small enough that the perturbations can be assumed spatially uniform, there are two orthogonal polarizations eigenmodes that are uncoupled. These modes define the so-called axes of birefringence of the fiber, having the property that the light preserves its polarization when it is injected parallel to them.

The amount of birefringence is characterized by the so-called polarization beat length  $L_B$ , defined as the propagation length over which the optical path length of the two polarization eigenmodes differs by exactly one wavelength (Fig. S3). This means that the phase difference between the two polarization eigenmodes linearly increases with propagation distance  $z$  as  $\phi = 2\pi z/L_B$ . If a linearly polarized light is injected at 45 degrees with respect to the linear polarization eigenmodes, the light acquires after one quarter of  $L_B$  a phase shift of  $\pi/2$ , transforming the input linear polarization into a circular one, and after one half of  $L_B$  a phase shift of  $\pi$ , transforming the input linear polarization into a linear polarization orthogonal to the input. Sections of fibers of the proper length are therefore equivalent to quarter-wave or a half-wave plates, both routinely used, in the laboratory, as polarization transformers.

However, being the source of birefringence in general not uniform along the fiber, the axes of birefringence and the birefringence itself are also not uniform. A long telecommunication fiber is therefore, to a good approximation, equivalent to a concatenation of polarization wave-plates with random orientation and random birefringence, of length equal to twice the typical length over which the birefringence decorrelates, usually referred to as the birefringence correlation length  $L_F$ . Both  $L_B$  and  $L_F$ , in modern day fibers, are of the order of meters (32).

The light polarization can be conveniently represented by Stokes vectors  $\vec{s}$ , which are unit vectors whose tips cover a unit sphere called the Poincaré sphere, embedded in a three-dimensional space called the Stokes space. The components of the Stokes vectors are the three

Stokes parameters of the field. The action of a section with constant birefringence  $\beta = 2\pi/L_B$  and length  $\Delta z$  can be represented in Stokes space as a rotation around a vector  $\vec{\beta}$ , called the birefringence vector, whose magnitude  $\beta$  multiplied by the length of the section  $\beta\Delta z = 2\pi\Delta z/L_B$  is equal to the rotation angle applied by the section, and whose direction is related to the orientation of the birefringence axes with respect to the reference frame of the fiber (33). The effect of the propagation across the whole fiber length can be then represented as the concatenation of multiple rotations around vectors of random magnitudes and orientations.

If the fiber is sitting in a quiet environment and not affected by time-dependent external perturbations, the Stokes vector of the output polarization  $\vec{s}_0$  is constant in time. When the fiber is instead exposed to a time dependent perturbation, e.g., stretch (34), twist (35), pressure (36), and bending (37), that couples to the fiber birefringence, the birefringence of each section of length  $2L_F$  changes and the Stokes vector of the output polarization  $\vec{s}(t)$  becomes time dependent. Sources of perturbation could be modulation of the hydrodynamical pressure experienced by the fiber, twist of the fiber, or strain caused by longitudinal stress.

Let  $N = L/(2L_F)$  be the total number of sections, centered at  $z_i = (2L_F)i$ , of a fiber link of length  $L$ . If  $\Delta\vec{\beta}(z_i, t)$  is the displacement of the birefringence caused by the perturbation, it may be shown that the change of the Stokes vector  $\Delta\vec{s}(t) = \vec{s}(t) - \vec{s}_0$  is the concatenation of  $N$  rotations around rotation vectors  $\Delta\vec{\beta}'(z_i, t)2L_F$ , where  $\Delta\vec{\beta}'(z_i, t)$  is the birefringence vector  $\Delta\vec{\beta}(z_i, t)$  rotated back by the static birefringence from  $z_i$  to the input (38). Because of the large number of sections, the vector  $\Delta\vec{\beta}'(z_i, t)$  is randomly oriented.

If  $|\Delta\vec{s}(t)| \ll 1$ , it may be shown that the displacement of the Stokes vector is, to first order,

$$\Delta\vec{s}(t) \cong \sum_{i=1}^N \Delta\vec{\beta}'(z_i, t)2L_F \times \vec{s}_0$$

This equation shows that the deviation of the Stokes vector from its static position is proportional to the sum of randomly oriented vectors of magnitude proportional to the birefringence perturbations.

In the measured data, the orientation of the Stokes vector is arbitrary, and sometimes slowly drifts because of time dependent external perturbations, mainly in the land section of the link. In order to separate the birefringence modulations originated by seismic events or ocean swells, we first perform a moving average of the measured Stokes signal over a 200s window,<sup>1</sup> and then digitally rotate the measured Stokes vector so as to align it to the third axis of the Stokes space,  $\vec{s}_0 = s_0\hat{e}_3$ . The 200-s window length is chosen to not impact the frequencies of interests in this study, higher than 10 mHz. After doing so, the Stokes vector displacement  $\Delta\vec{s}(t)$  has only two non-zero components, that is  $\Delta\vec{s}(t) = s_1(t)\hat{e}_1 + s_2(t)\hat{e}_2$ . The two quantities  $s_1(t)$  and  $s_2(t)$  are therefore equal to the components along the first and second axis of the Stokes space of the birefringence perturbation  $\sum_{i=1}^N \Delta\vec{\beta}'(z_i, t)2L_F$ . The third component is statistically equivalent to the first two for the isotropy of  $\Delta\vec{\beta}'(z_i, t)$ .

---

<sup>1</sup> The width of this window sets a low frequency limit to detectable seismic events. Being determined by the time scale of the slow polarization drift, longer averaging windows are sufficient in systems with a more stable polarization, which would allow pushing the low frequency limit down to smaller values.

Being the relation that links  $s_1(t)$  and  $s_2(t)$  to the birefringence perturbation linear, filtering  $s_1(t)$  and  $s_2(t)$  is equivalent to filtering the components orthogonal to the third Stokes axis of the accumulated birefringence perturbation  $\sum_{i=1}^N \Delta\vec{\beta}'(z_i, t)$ . Consequently, because of the isotropy of  $\Delta\vec{\beta}'(z_i, t)$ , the integrated power spectral density of  $s_1(t)$  and  $s_2(t)$  is proportional on average to  $\int E[|\sum_{i=1}^N \Delta\vec{\beta}'(z_i, t)|^2 dt]$  which, because of the random orientation of the birefringence perturbations, is equal to  $\int \sum_{i=1}^N E[|\Delta\vec{\beta}'(z_i, t)|^2] dt$  where with  $E[\cdot]$  we denote ensemble averaging over the random static fiber birefringence. This relation gives a quantitative estimate of the strength of the birefringence perturbation by the fluctuations of the Stokes vector of the output polarization of the link.

The use of polarization monitoring in geophysical sensing may pose challenges because of the non-obvious interpretation of the signal, and this technique also suffers from the limitations arising from its finite dynamic range. However, this approach also shows a distinct advantage over that based on the detection of the absolute phase of an ultra-stable laser field, beside of course the obvious one that is the scalability of the method. Indeed, polarization detection is, in essence, equivalent to the measurement of the phase difference between two orthogonally polarized fields and hence it is intrinsically transparent to the noise of the common phase of the optical carrier. Consequently, polarization measurements are immune to the low-frequency noise, proportional to  $1/f^2$ , that instead affects the absolute phase of a laser field, which originates from the random-walk of the laser phase (or, equivalently, from a white-noise of the laser frequency) (39). This immunity is confirmed by the flat low frequency spectrum in back-to-back configuration shown in Fig. 3C of the main text. In the same figure, it is also shown that the power spectral density of the polarization deviations approximately grows, after 10,000 km, proportionally to  $1/f$ . Although the interpretation of this signature awaits further investigations, it should be mentioned that this contribution could hardly be detected without a flat polarization noise spectrum at low frequency. In addition, it should be noted that a limited low-frequency noise was essential for the clear detection of the ocean wave signature in the primary microseism band shown in Fig. 4 of the main text.

In our detection procedure, the fluctuations of the SOP were defined with respect to a mean SOP trace calculated with a 200-s moving window, and this procedure sets a limit to the low frequency bandwidth of the measurement. The moving window was used to separate the signal from a long-term polarization drift of the received signal. This drift arises because the Curie cable was not designed for polarization monitoring, so that no special care was taken to achieve polarization stability over long time scales (of the order of minutes). In modern communication systems, polarization is tracked at GHz rate by the digital signal processing that follows coherent detection, so that slow polarization drifts do not affect the transmission performance in any significant way and, hence, no attention is paid to avoid them. The receiver signal of the Curie system experiences a slow polarization drift that is likely to be generated by environmental perturbations in the unprotected environment of the terminal stations (on and off switching of the air conditioning, to mention only one). More research is needed to reduce or compensate the long-period SOP noise, without affecting the system design and operation substantially.

Reconstruction of polarization and phase with optical hybrids was described in reference (40) for metrological applications based on 50-km long in-field fiber. A physical model has not been established yet to interpret our coherent SOP measurements (e.g., amplitudes and waveform shapes) quantitatively. We do not address polarization-induced phase noise, but present

experimental observation where miniscule changes due to earthquake induce optical phase changes with pronounced SOP excursion at the coherent receiver.

## Measurements of SOP and channel configurations

Our method to extract the state of polarization of an optical signal travelling through the undersea cable is based on the use of commercially available transponders operating at transmission speeds of 100Gb/s and beyond based on coherent detection (20,41). At the transmitter side, we modulate a C-band low-linewidth laser using a dual polarization in-phase and quadrature Mach-Zehnder modulator. Our 4-dimensional signal (in-phase and quadrature components of two orthogonal polarizations) is then amplified and launched in the fiber with other channels using wavelength multiplexing. At the receiver side we optically filter the desired channel and use a coherent detector to down-convert it resulting in 4 electrical signals which are sampled by high-speed analog-to-digital converters. The 4 signals correspond to the in-phase and quadrature components of two orthogonal polarizations and is a direct map of the optical signal that arrives at the receiver after fiber transmission (with phase and polarization relative to the absolute phase and polarization of the coherent receiver).

To recover the transmitted signal, the receiver needs to first estimate and compensate for several impairments due to transmission with digital signal processing. The impairments are: clock difference between transmitter and receiver, chromatic dispersion, polarization effects (polarization mode dispersion, polarization offset between transmitter and receiver) and optical phase recovery (difference in phase and frequency between transmitter laser and receiver local oscillator). For a detailed description of these effects and signal processing algorithms to estimate and compensate them, see (18).

The digital signal processing step we are interested in this work is the adaptive equalizer which deals with the compensation of the dynamic polarization to separate the independent signals coming from the two orthogonal polarizations. The time-domain adaptive equalizer is defined by:

$$\begin{bmatrix} y_H \\ y_V \end{bmatrix} = \begin{bmatrix} w_{HH}^T & w_{VH}^T \\ w_{HV}^T & w_{VV}^T \end{bmatrix} \begin{bmatrix} x_H \\ x_V \end{bmatrix}.$$

The equalizer consists of four filters in a butterfly structure with L coefficients per filter in the form  $w_{\{in\}\{out\}}$ , where the subscripts are the horizontal (H) and vertical (V) polarizations. The non-equalized inputs (where polarizations are mixed) are 2 vectors with length L ( $x_V$  and  $x_H$ ) usually at 2 samples-per-symbol. The 1 sample-per-symbol output signals  $y_V$  and  $y_H$  are the equalized polarization-separated signals. Note that all the signals here are complex-valued time-varying but we omit time subscripts in the equation for simplicity. The equalizers are updated as follows:

$$w_{\{in\}\{out\},k+1} = w_{\{in\}\{out\},k} - \mu \frac{\partial e(y_{\{out\},k})}{\partial w_{\{in\}\{out\},k}},$$

where  $\mu$  controls the speed of the equalizer and  $e(y)$  is an error function to be minimized and is typically based on the constant modulus algorithms (CMA) and its variants. For the CMA  $e(y) = (1 - |y|^2)^2$ . A working equalizer results in correct tracking of the dynamic polarization effects which impair the signal through transmission. The goal of our approach is to extract from the 4 filters the state of polarization information. Since the polarization content is frequency independent (first-order approximation), we can focus on the frequency-domain response of the

filters denoted  $W_{\{in\}\{out\}}(f)$  and work with the polarization at the center of the channel ( $f = 0$ ). To extract the Stokes parameters from the equalizers, we follow (42) and for one of the two (H or V) input linear polarizations, we obtain:

$$\begin{aligned}
 S_0 &= |W_{HH}(0)|^2 + |W_{VH}(0)|^2, \\
 S_1 &= (|W_{HH}(0)|^2 - |W_{VH}(0)|^2)/\sqrt{S_0}, \\
 S_2 &= (|W_{HH}(0)||W_{VH}(0)|\cos(\angle(W_{HH}(0)\bar{W}_{VH}(0))))/\sqrt{S_0}, \\
 S_3 &= (|W_{HH}(0)||W_{VH}(0)|\sin(\angle(W_{HH}(0)\bar{W}_{VH}(0))))/\sqrt{S_0}.
 \end{aligned}$$

These signals (S1, S2 and S3) are on the surface of the unit sphere and are used to detect the earthquake. Note that these filters are computed continually at Gigahertz speeds using application specific integrated circuits (ASICs) to be able to demodulate signals operating in the hundreds of Gigabit/s. Using commercial hardware, we are limited by the reading speed of CPUs to access these coefficients, however sampling rates of 10s of Hz are sufficient for the detection of earthquakes which show up in below 2 Hz in the spectrum.

### SOP timing mechanism

In the early phase of our experiment, we timestamped the SOP output from the commercial coherent transponders based on the system time in the microcontroller, NTP synchronized. However, the data collection pipeline is asynchronous with processing delays that depend on the random utilization of the microcontroller during the normal operation of the transponder. For this reason, the SOP measurement timing can be affected by a random inaccuracy of the order of a few ms, even accumulative up to seconds or minutes depending on the implementation of the collection software (e.g., frequency of re-synchronization with the remote NTP server). For example, Fig. S12 shows the SOP detection of the 28 March 2020, M4.4 earthquake that was at a close distance to the Curie cable. The signal is delayed by about 30 s compared with the theoretical P and S arrival times. Throughout the experiment we have improved the collection software to reduce the inaccuracy down to the order of ms consistently. In the future, more accurate timing mechanisms (e.g., GPS clock synchronization) could enable earthquake localization via delayed bi-directional SOP measurements.

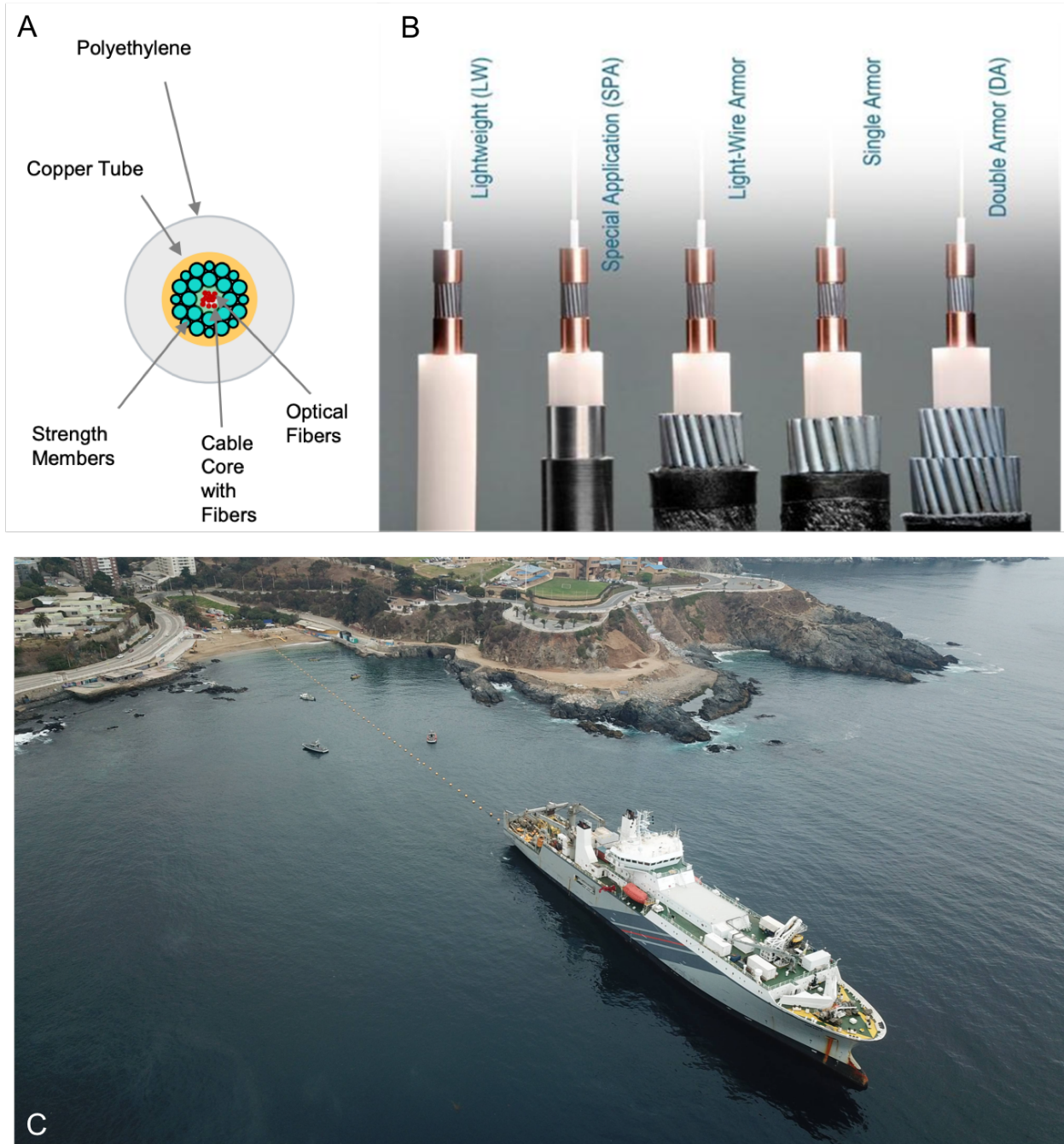


**Figure S1.** Structure and types of the cables used in the Curie cable. (A) Lightweight (LW) optical fiber cable with steel strand wire configuration. The interlocking strength members resist external pressure up to 8,000 meter water depth. LW cable (95% of Curie length is LW) has external diameter 17 mm and weight in air 4.8 kN/km. Cable core with fibers consists of a polyethylene tube filled with gel. (B) Armored part of the Curie cable (5%) consists of Special Application, Light-Weight Armor, and Double Armor cable. (C) The landing point of cable Curie at Valparaiso, Chile. In this photo, the big ship was deploying the Curie cable, whose path can be seen along the line of floats behind the ship.

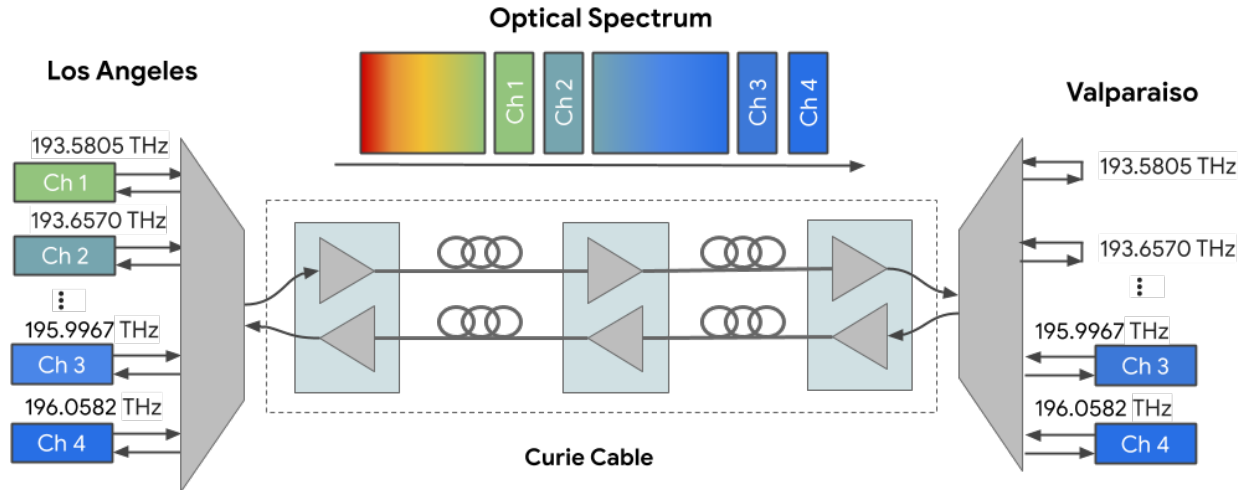


**Figure S2.** Topology of SOP sensing on the Curie cable. A series of coherent transponders operating at different optical frequencies is connected to a muxing/demuxing device (the trapezoids) which is then connected to the Curie cable. The transponders are used to transmit and receive data to/from Los Angeles and Valparaiso over a fiber pair in Curie. Two transponders (Channel 1 and Channel 2) are connected in loop-back configuration as the signal is transmitted and received in Los Angeles. The other transponders, either in Los Angeles or Valparaiso, can be used to determine the SOP of the received optical field. Channels in the optical spectrum can be interleaved with ASE (Amplified Spontaneous Emission) noise to maintain a constant spectral load in the subsea cable. We have four channels in our current SOP sensing setup, at four frequencies through one strand of fiber. With the 4 fiber pairs in Curie and ~50 available frequencies per fiber pair, we can potentially open 200 bidirectional channels along Curie.

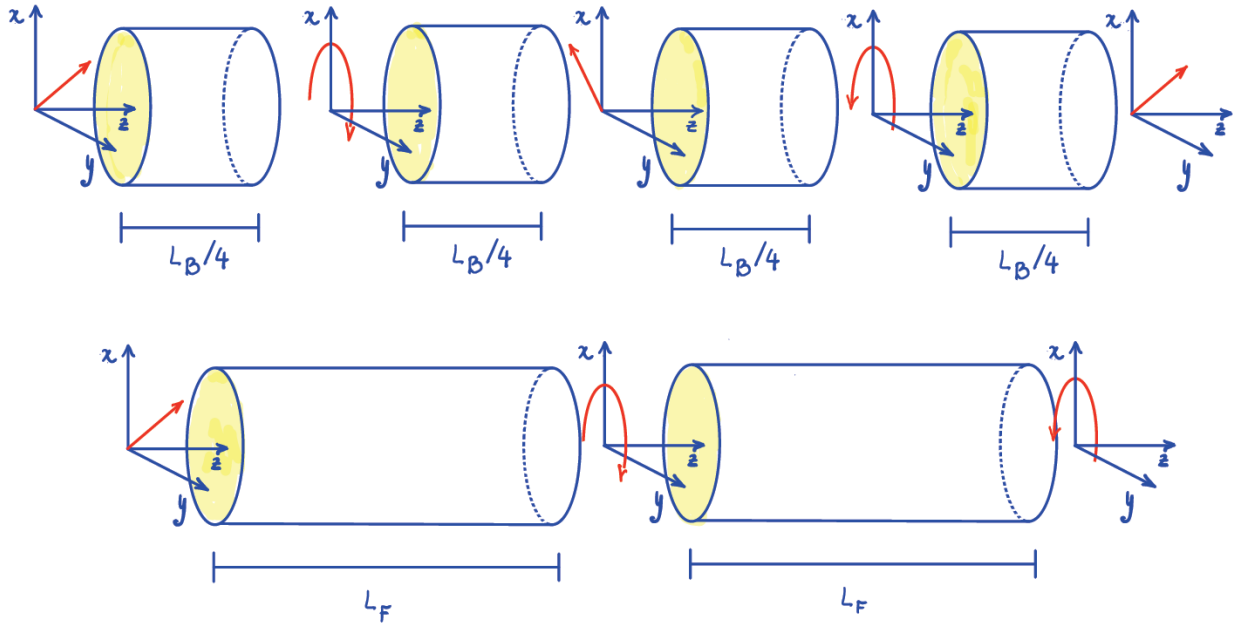


**Figure S3.** Upper panel: schematic representation of a fiber section of constant birefringence, with birefringence axes parallel to  $x$  and  $y$ . Over a birefringence beat length  $L_B$ , the polarization experiences a full cyclic evolution from linear polarization at  $45^\circ$  to the birefringence axes to, say, right hand circular polarization after  $L_B/4$ , back to linear polarization but orthogonal to the input after  $L_B/2$ , to left hand circular polarization after  $3L_B/4$  and back to the input polarization after  $L_B$ . Lower panel: concatenation of two fiber sections with arbitrary orientation of the birefringence axes of length equal to the birefringence correlation length  $L_F$ . For any input polarization, here linear, the polarization, after propagation through a few sections of length  $L_F$ , becomes arbitrary and random.

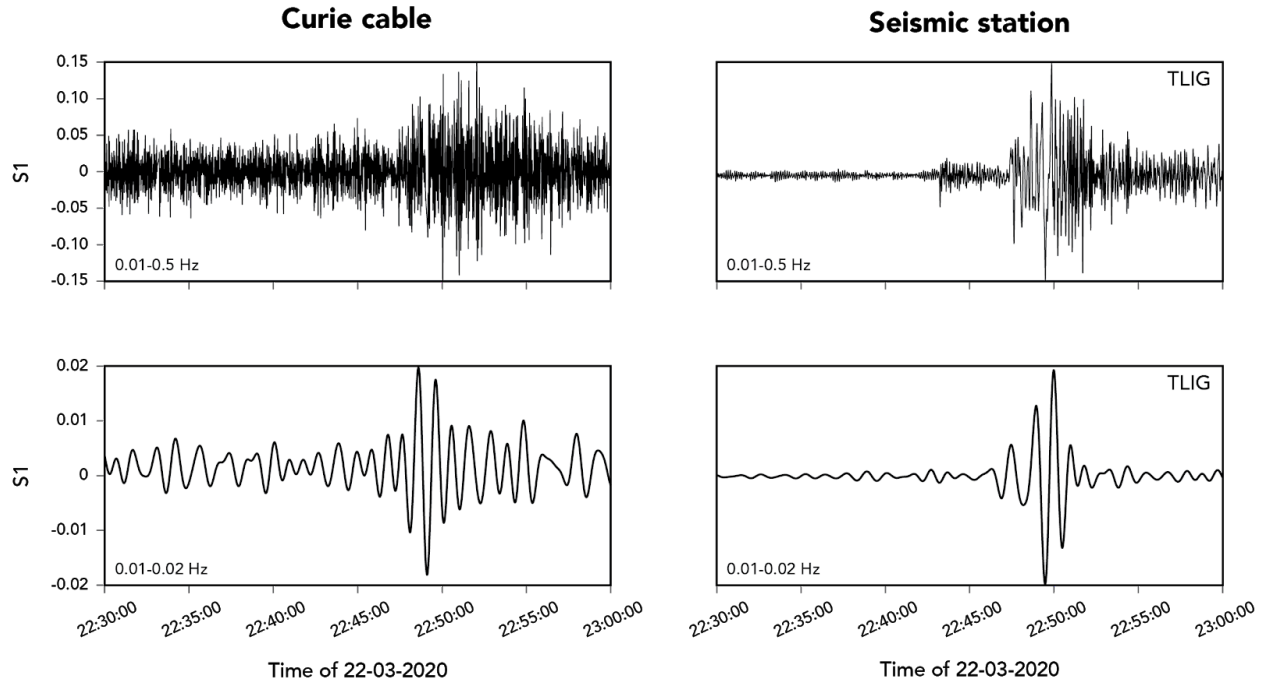


**Figure S4.** Detection of far-field long-period surface waves on SOP. Stokes parameter S1 (left) together with seismograms at conventional seismic station TLIG (right) for the 22 March 2020 Mw 6.1 earthquake on the central East Pacific Rise (Fig. 1). Station TLIG has a similar epicentral distance as the closest point along the Curie cable. The relatively broadband SOP S1 data (0.01-0.5 Hz) in the top row are noisy, but the low frequency surface wave (0.01-0.02 Hz; bottom) is detected clearly on SOP, with a slightly earlier arrival time than on TLIG because of distance differences.

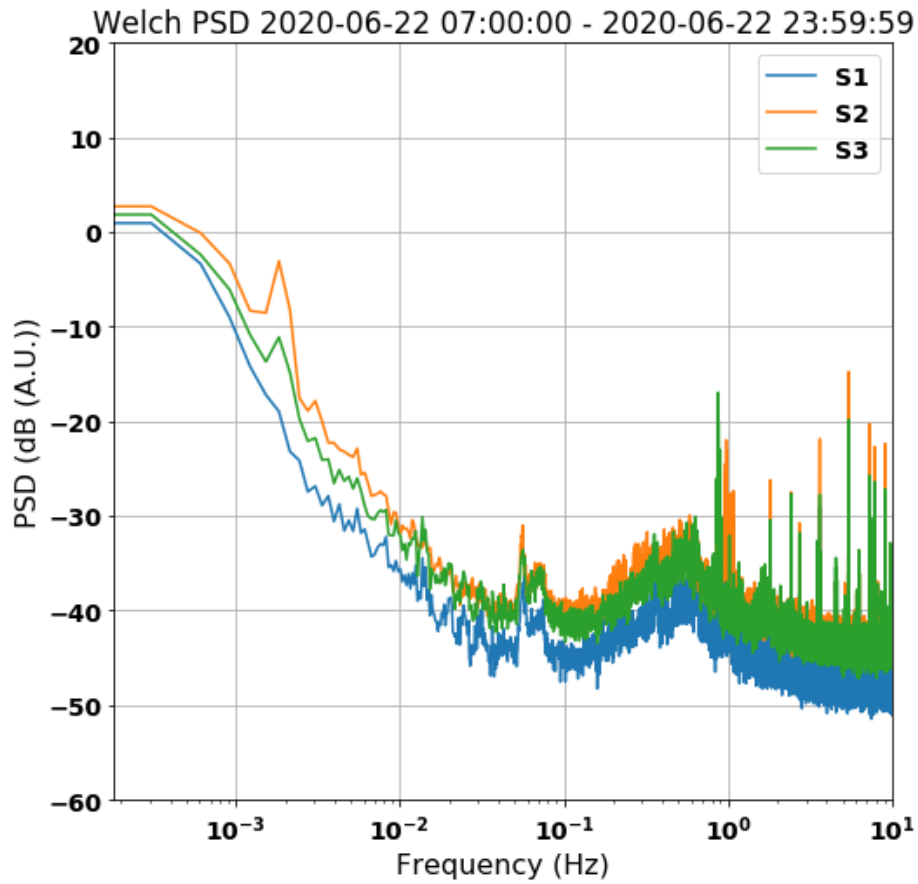


**Figure S5.** Noise Power Spectral Density (PSD) between 0.2 mHz and 10 Hz. Here S1, S2, and S3 are the original Stokes parameters without rotation over 200-s moving windows (Fig. 2C). Therefore, the input preserves the long period energy. Welch's method is used in computing the PSD, with a moving window length of 54.6 minutes.

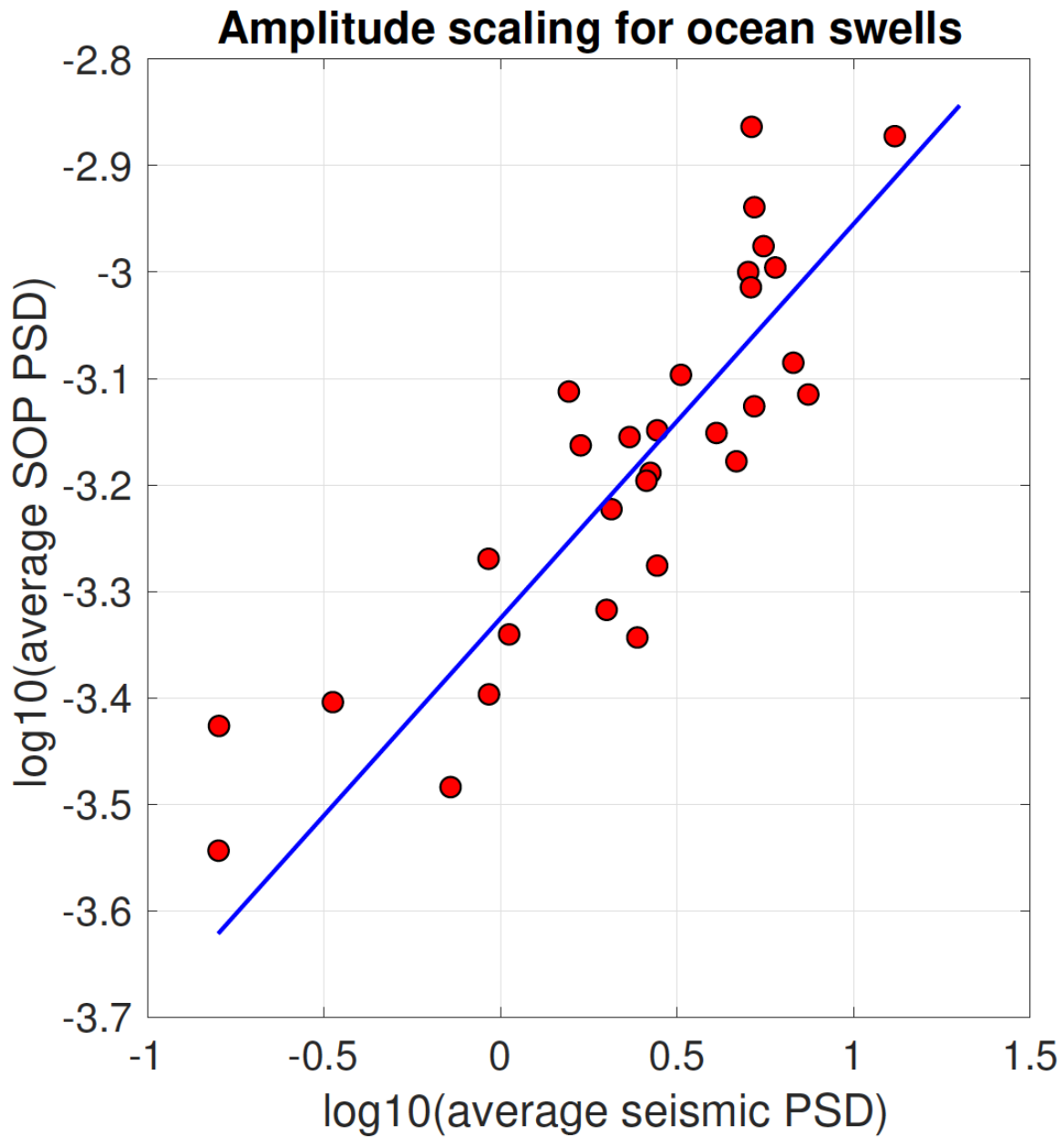


**Figure S6.** SOP amplitude scaling for about 30 ocean swell events throughout the test period. The primary microseism strength on SOP is defined as the median PSD for individual dispersive events, while the secondary microseism strength is defined as the median relative PSD at station SLBS for each ocean swell.

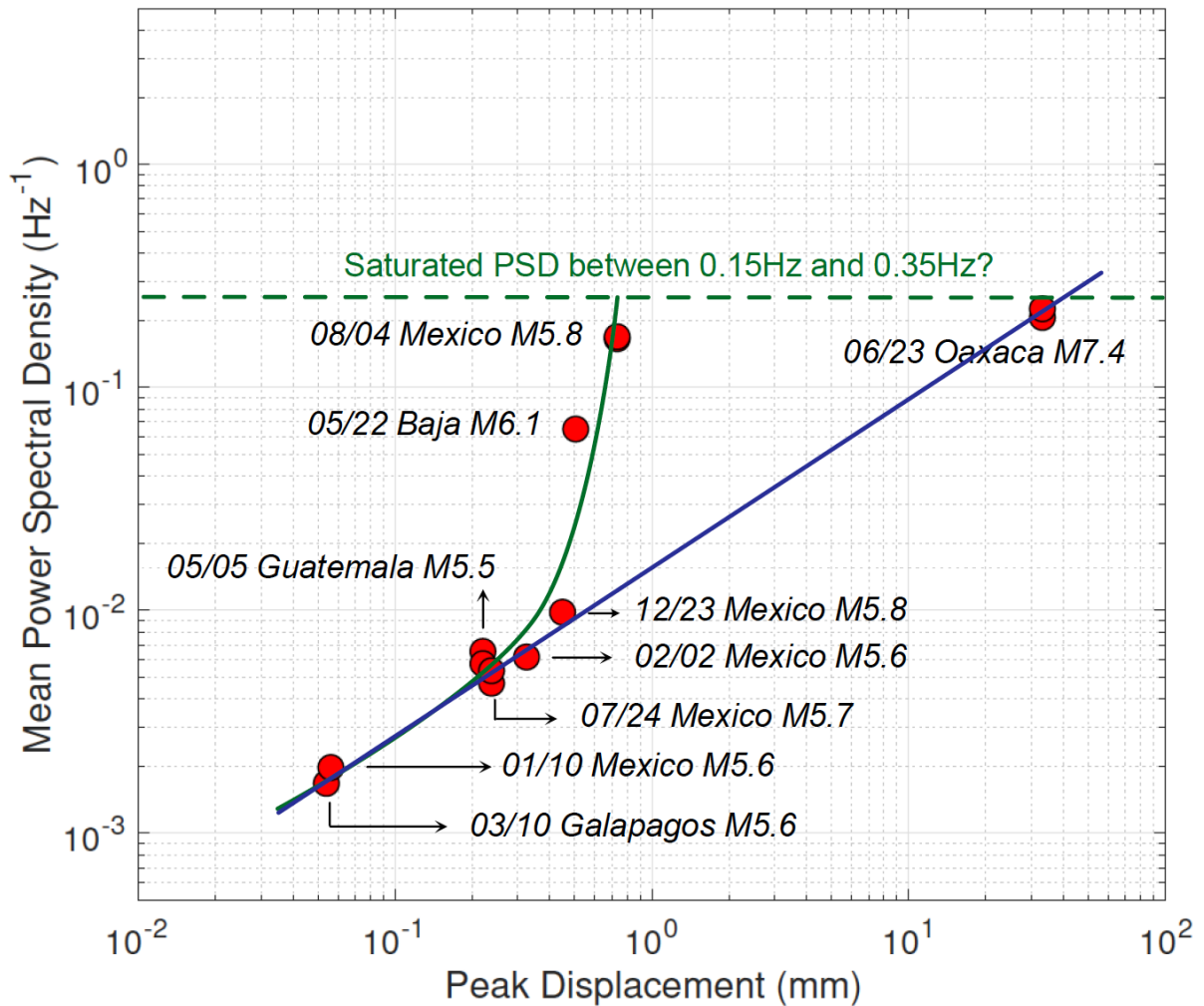


**Figure S7.** Amplitude scaling for earthquakes. Multiple earthquakes along the central American section of Curie detected in our SOP records (Figure 1), allowing us to explore an empirical scaling of the SOP amplitudes and ground shaking, while most other factors are kept nearly constant (e.g., Earth structure, fiber coupling and orientations). Similar to the Mw 7.4 earthquake, the central American events consistently show an energy peak between 0.15 and 0.35 Hz. We therefore measured the average power spectral density (PSD) of the peak within the first 5 minutes of the earthquake-induced signals as a proxy of the SOP amplitudes. We found that the mean PSDs scale in general correlates with the predicted peak displacement along Curie (red dots), assuming the GCMT source parameters and a 1D IASPEI Earth model. We propose two models. (1) A power-law scaling with the exponent close to 1 between the mean PSD and peak displacement (blue line). In this model the 05/22 Baja M6.1 and the 08/04 Mexico 5.8 earthquakes are outliers, potentially because of some unique properties of the two events (e.g., strong excitation of water waves). (2) A non-linear model that has saturated SOP response when the peak displacement is over 1 mm (green solid and dashed lines). However, without more data, it is not yet possible to reject either models, or propose a different scaling that considers other measured quantities, potentially in a different frequency band.

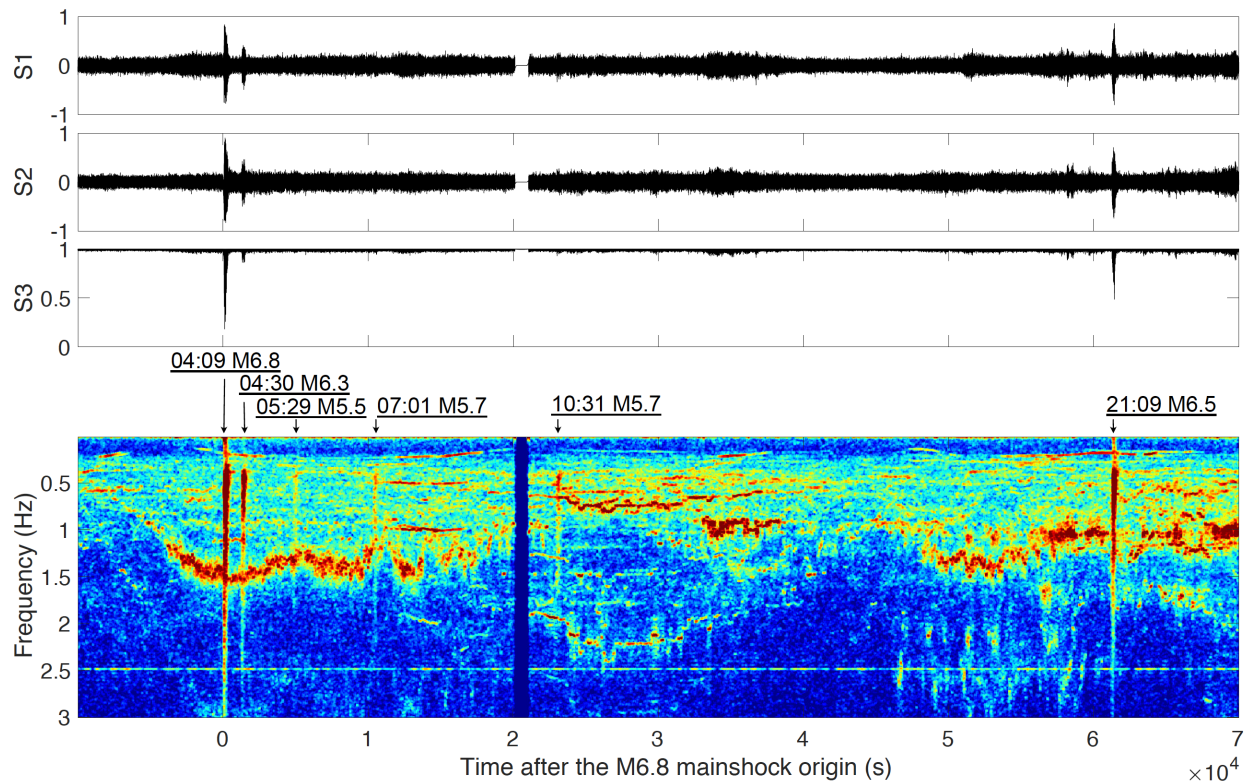


**Figure S8.** SOP signals of the 01 September 2020 M6.8 submarine earthquake offshore Vallenar, Chile and its aftershock sequence within about one day. S1, S2, and S3 are the Stokes parameters after rotation (Fig. 2). Five of the largest aftershocks can be clearly identified as near vertical energy stripes on the spectrogram. The amplitudes of the S3 component appears to scale well with the earthquake sizes for the three largest events: 04:09 M6.8 mainshock, 04:30 M6.3 and 21:09 M6.5 aftershocks.

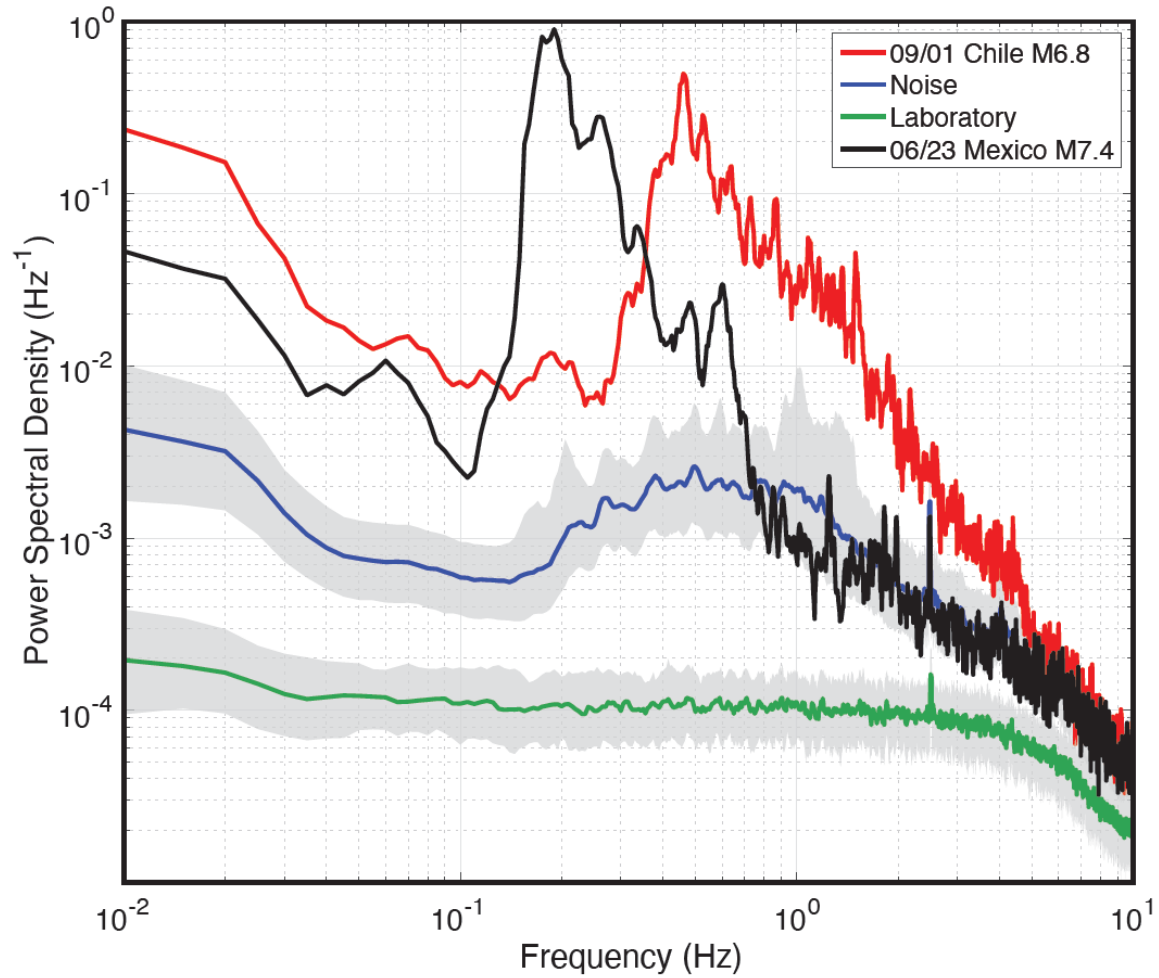


**Figure S9.** Similar as Fig. 3C, but for the 01 September 2020 M6.8 Chile earthquake (Fig. S8). The calculation of power spectral density (PSD) follows the approaches by McNamara and Boaz (43), except with a short time window of 200s. The PSD of the 23 June 2020 M7.4 Mexico earthquake is shown here for comparison to illustrate the differences in frequency content.

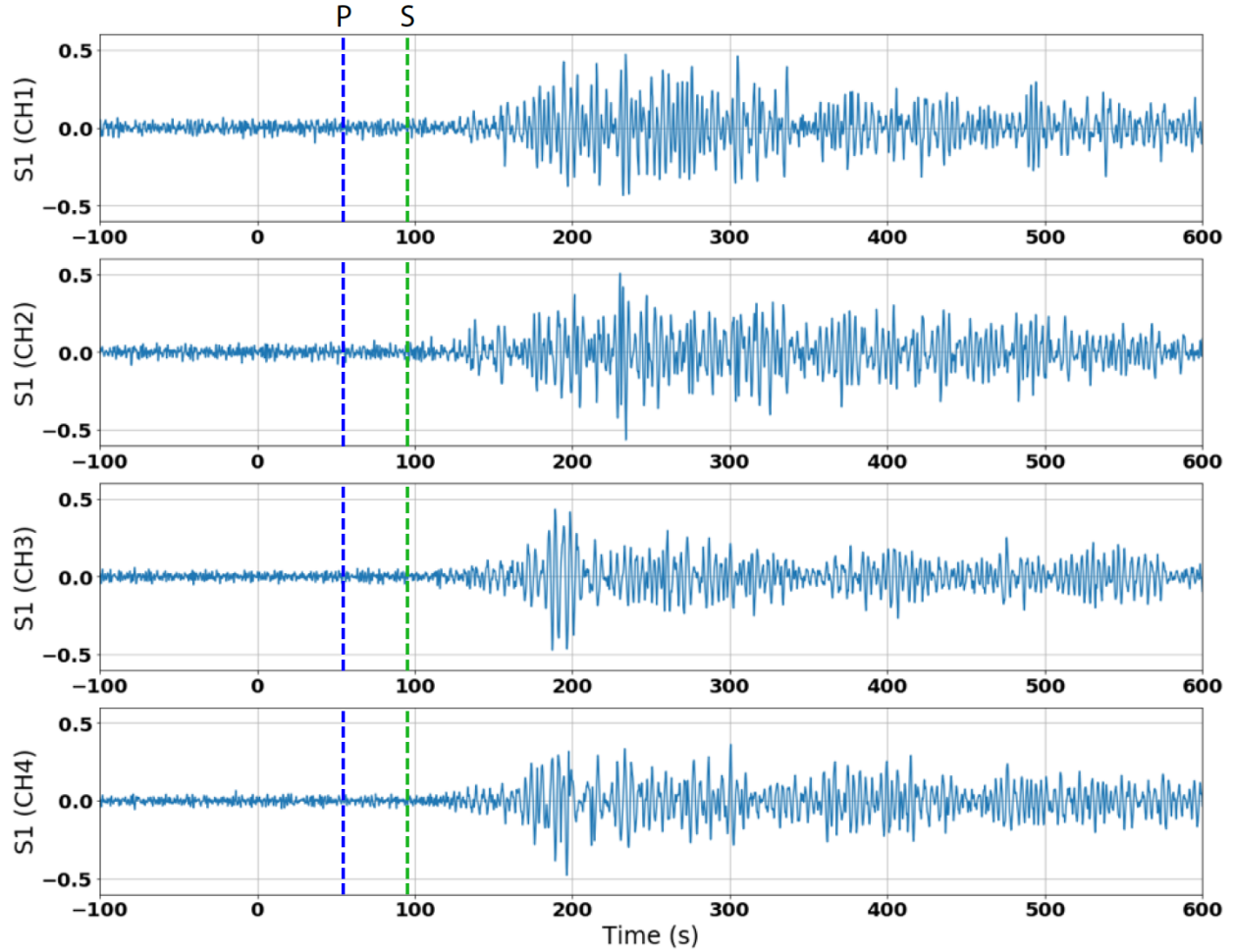


**Figure S10.** SOP Detection of the 04 August 2020 19:17:52 M5.8 submarine earthquake offshore Guatemala. The earthquake is about 400 km to the Curie cable at the closest point, while about 100 km to the Guatemalan coast. The seismic waves were detected above noise on Curie about 130s after the earthquake origin time on all four monitoring channels as described in Fig. S2. The S1 waveforms have been filtered between 0.1 to 0.8 Hz. Note that CH1 with CH2, and CH3 with CH4 show visibly a much higher similarity, than between the two couples of channels, as expected for the separation of 2.5 THz between the two couples, whereas each element of the couple is separated by only 76.5 GHz (CH1-CH2) and 61.5 GHz (CH3-CH4). This is consistent with the fact that the correlation function of the output Stokes vector drops by 3dB for, given the PMD of the Curie link of 3ps, for a frequency separation of 70 GHz (44,45). It is therefore appropriate to consider the channels separated by much more than 70 GHz to be independent realizations of the fixed random birefringence, because of the ergodicity in frequency of the birefringence (46, 47). Combining the SOP traces of these channels (e.g., by stacking the power envelopes) might therefore reduce the uncertainty due to the stochastic nature of the birefringence.

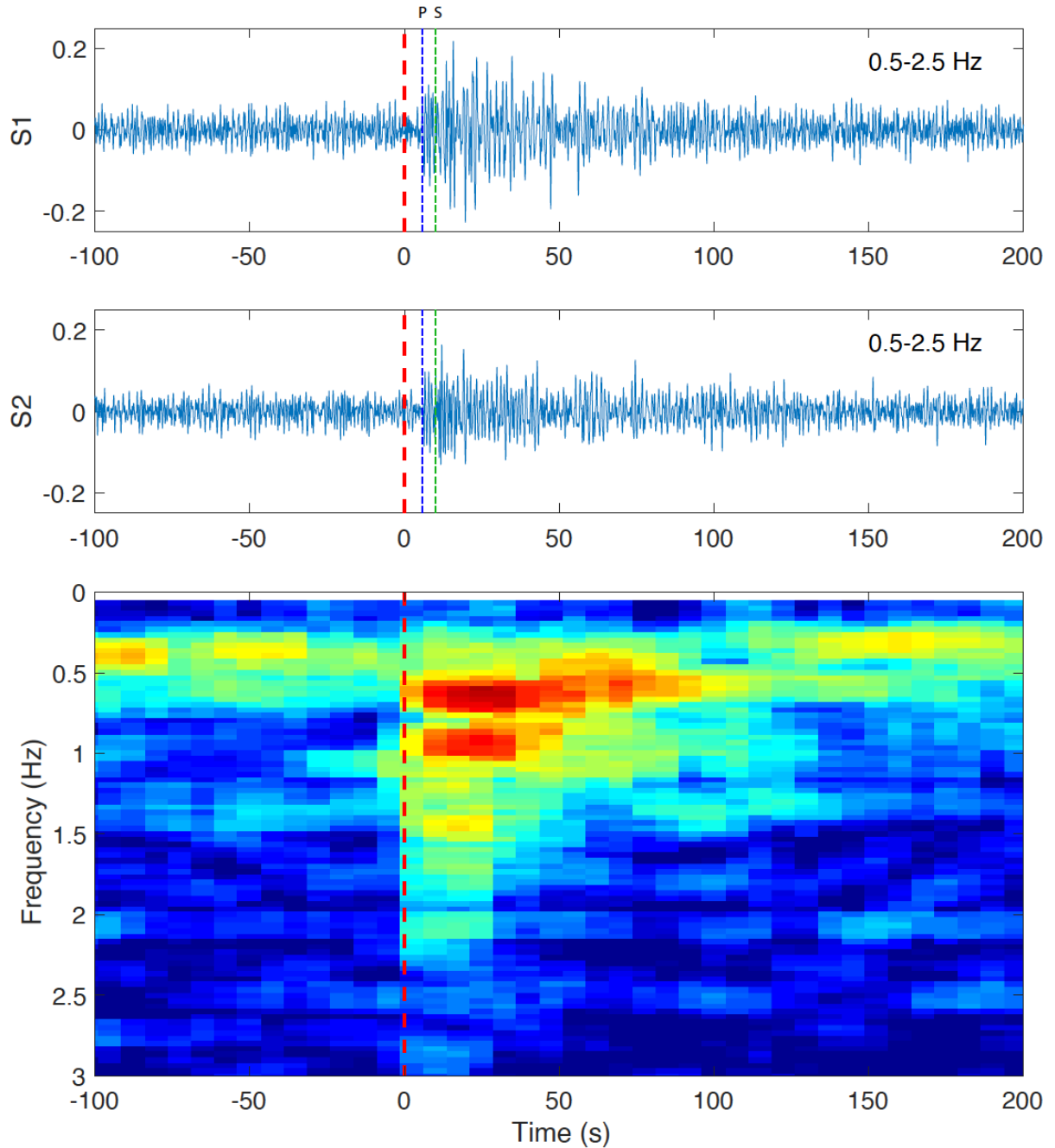


**Figure S11.** SOP Detection of the 14 August 2020 09:30:50 M5.3 submarine earthquake offshore Mexico. The earthquake is about 35 km to the Curie cable at the closest point, while about 200km to the Mexico coast. The seismic waves were detected on Curie about 6s after the earthquake origin time, while the closest seismic station with data available from IRIS, MOIG, was 520 km away and registered P wave 64s later. The red, blue, and green dashed lines are earthquake origin time and predicted P and S arrival times, respectively, from the earthquake to the closest point along the Curie cable.

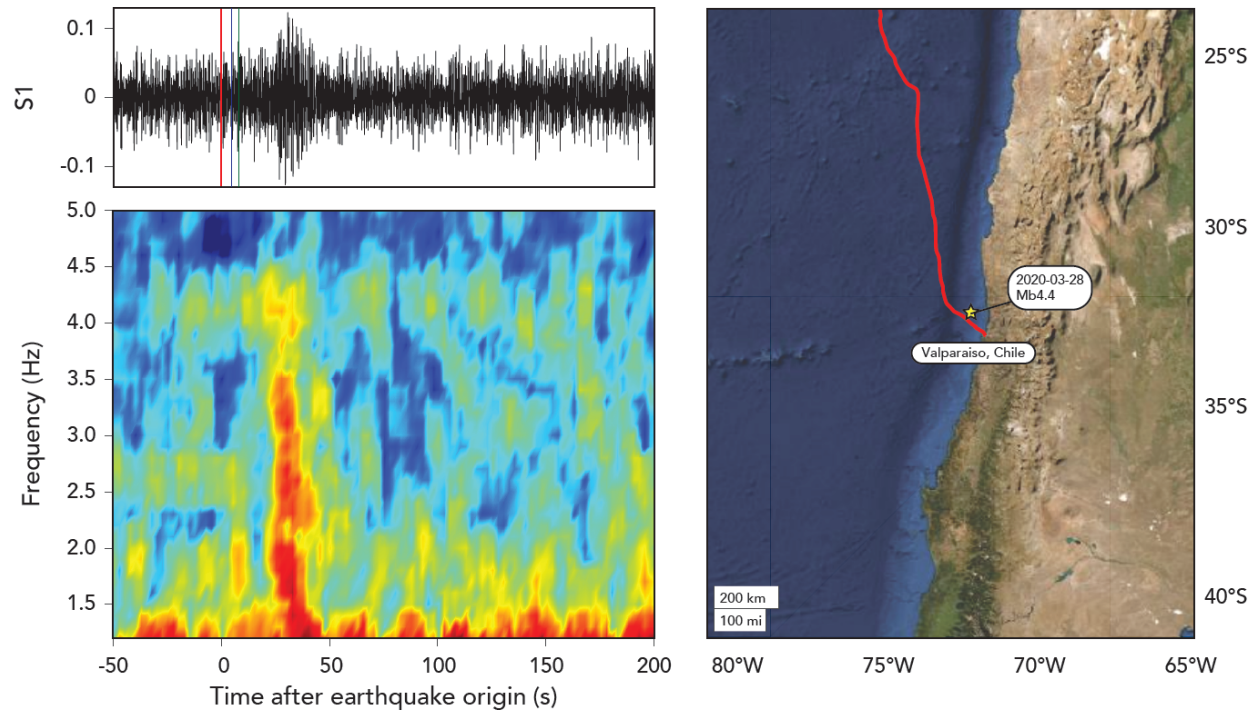


**Figure S12.** Detection of the 28 March 2020, M4.4 earthquake near Valparaiso, close to the Curie cable (red line) as shown by the right panel. The left panel shows the raw S1 component of the Stokes parameters and its spectrogram between 1.5 and 5 Hz. The red, blue, and green lines in the topleft panel are earthquake origin time and predicted P and S arrival times, respectively, from the earthquake to the closest point along the Curie cable. The SOP signal of the earthquake is about 30s later than the predicted arrival times, which we believe is caused by SOP clock issues in the early stage of our experiment.

## References and Notes

1. D. Suetsugu, H. Shiobara, Broadband ocean-bottom seismology. *Annu. Rev. Earth Planet. Sci.* **42**, 27–43 (2014). [doi:10.1146/annurev-earth-060313-054818](https://doi.org/10.1146/annurev-earth-060313-054818)
2. R. Bürgmann, D. Chadwell, Seafloor geodesy. *Annu. Rev. Earth Planet. Sci.* **42**, 509–534 (2014). [doi:10.1146/annurev-earth-060313-054953](https://doi.org/10.1146/annurev-earth-060313-054953)
3. G. Nolet, Y. Hello, S. Lee, S. Bonnieux, M. C. Ruiz, N. A. Pazmino, A. Deschamps, M. M. Regnier, Y. Font, Y. J. Chen, F. J. Simons, Imaging the Galápagos mantle plume with an unconventional application of floating seismometers. *Sci. Rep.* **9**, 1326 (2019). [doi:10.1038/s41598-018-36835-w](https://doi.org/10.1038/s41598-018-36835-w) [Medline](#)
4. G. Marra, C. Clivati, R. Luckett, A. Tampellini, J. Kronjäger, L. Wright, A. Mura, F. Levi, S. Robinson, A. Xuereb, B. Baptie, D. Calonico, Ultrastable laser interferometry for earthquake detection with terrestrial and submarine cables. *Science* **361**, 486–490 (2018). [doi:10.1126/science.aat4458](https://doi.org/10.1126/science.aat4458) [Medline](#)
5. E. F. Williams, M. R. Fernández-Ruiz, R. Magalhaes, R. Vanthillo, Z. Zhan, M. González-Herráez, H. F. Martins, Distributed sensing of microseisms and teleseisms with submarine dark fibers. *Nat. Commun.* **10**, 5778 (2019). [doi:10.1038/s41467-019-13262-7](https://doi.org/10.1038/s41467-019-13262-7) [Medline](#)
6. A. Sladen, D. Rivet, J. P. Ampuero, L. De Barros, Y. Hello, G. Calbris, P. Lamare, Distributed sensing of earthquakes and ocean-solid Earth interactions on seafloor telecom cables. *Nat. Commun.* **10**, 5777 (2019). [doi:10.1038/s41467-019-13793-z](https://doi.org/10.1038/s41467-019-13793-z) [Medline](#)
7. N. J. Lindsey, T. C. Dawe, J. B. Ajo-Franklin, Illuminating seafloor faults and ocean dynamics with dark fiber distributed acoustic sensing. *Science* **366**, 1103–1107 (2019). [doi:10.1126/science.aay5881](https://doi.org/10.1126/science.aay5881) [Medline](#)
8. Z. Zhan, Distributed acoustic sensing turns fiber-optic cables into sensitive seismic antennas. *Seismol. Res. Lett.* **91**, 1–15 (2020). [doi:10.1785/0220190112](https://doi.org/10.1785/0220190112)
9. B. M. Howe, B. K. Arbic, J. Aucan, C. R. Barnes, N. Bayliff, N. Becker, R. Butler, L. Doyle, S. Elipot, G. C. Johnson, F. Landerer, S. Lentz, D. S. Luther, M. Müller, J. Mariano, K. Panayotou, C. Rowe, H. Ota, Y. T. Song, M. Thomas, P. N. Thomas, P. Thompson, F. Tilmann, T. Weber, S. Weinstein, SMART cables for observing the global ocean: Science and implementation. *Front. Mar. Sci.* **6**, 424 (2019). [doi:10.3389/fmars.2019.00424](https://doi.org/10.3389/fmars.2019.00424)
10. Materials and methods are available as supplementary materials.
11. H. Kanamori, L. Rivera, S. Lambotte, Evidence for a large strike-slip component during the 1960 Chilean earthquake. *Geophys. J. Int.* **218**, 1–32 (2019). [doi:10.1093/gji/ggz113](https://doi.org/10.1093/gji/ggz113)
12. H. Eissler, L. Astiz, H. Kanamori, Tectonic setting and source parameters of the September 19, 1985 Michoacan, Mexico earthquake. *Geophys. Res. Lett.* **13**, 569–572 (1986). [doi:10.1029/GL013i006p00569](https://doi.org/10.1029/GL013i006p00569)
13. M. Born, E. Wolf, *Principles of Optics: Electromagnetic Theory of Propagation, Interference and Diffraction of Light* (Elsevier, 2013).

14. J. Wuttke, P. M. Krummrich, J. Rösch, Polarization oscillations in aerial fiber caused by wind and power-line current. *IEEE Photonics Technol. Lett.* **15**, 882–884 (2003). [doi:10.1109/LPT.2003.811143](https://doi.org/10.1109/LPT.2003.811143)
15. P. M. Krummrich, E.-D. Schmidt, W. Weiershausen, A. Mattheus, “Field trial results on statistics of fast polarization changes in long haul WDM transmission systems,” *Optical Fiber Communication Conference and Exposition and The National Fiber Optic Engineers Conference Technical Digest* (paper OThT6, Optical Society of America, 2005).
16. D. Charlton, S. Clarke, D. Doucet, M. O’Sullivan, D. L. Peterson, D. Wilson, G. Wellbrock, M. Bélanger, Field measurements of SOP transients in OPGW, with time and location correlation to lightning strikes. *Opt. Express* **25**, 9689–9696 (2017). [doi:10.1364/OE.25.009689](https://doi.org/10.1364/OE.25.009689) [Medline](#)
17. S. G. Evangelides, L. F. Mollenauer, J. P. Gordon, N. S. Bergano, Polarization multiplexing with solitons. *J. Lightwave Technol.* **10**, 28–35 (1992). [doi:10.1109/50.108732](https://doi.org/10.1109/50.108732)
18. S. J. Savory, Digital coherent optical receivers: Algorithms and subsystems. *IEEE J. Sel. Top. Quantum Electron.* **16**, 1164–1179 (2010). [doi:10.1109/JSTQE.2010.2044751](https://doi.org/10.1109/JSTQE.2010.2044751)
19. G. Charlet, J. Renaudier, H. Mardoyan, P. Tran, O. B. Pardo, F. Verluise, M. Achouche, A. Boutin, F. Blache, J.-Y. Dupuy, S. Bigo, Transmission of 16.4-bit/s capacity over 2550 km using PDM QPSK modulation format and coherent receiver. *J. Lightwave Technol.* **27**, 153–157 (2009). [doi:10.1109/JLT.2008.2005506](https://doi.org/10.1109/JLT.2008.2005506)
20. C. R. S. Fludger, T. Duthel, D. van den Borne, C. Schulien, E.-D. Schmidt, T. Wuth, J. Geyer, E. De Man, Khoe Giok-Djan, H. de Waardt, Coherent equalization and POLMUX-RZ-DQPSK for robust 100-GE transmission. *J. Lightwave Technol.* **26**, 64–72 (2008). [doi:10.1109/JLT.2007.912128](https://doi.org/10.1109/JLT.2007.912128)
21. M. Vallée, Source time function properties indicate a strain drop independent of earthquake depth and magnitude. *Nat. Commun.* **4**, 2606 (2013). [doi:10.1038/ncomms3606](https://doi.org/10.1038/ncomms3606) [Medline](#)
22. E. A. Okal, The generation of *T* waves by earthquakes. *Adv. Geophys.* **49**, 1–65 (2008). [doi:10.1016/S0065-2687\(07\)49001-X](https://doi.org/10.1016/S0065-2687(07)49001-X)
23. Y. Zheng, X. Fang, J. Liu, M. C. Fehler, Scholte waves generated by seafloor topography. [arXiv:1306.4383](https://arxiv.org/abs/1306.4383) [physics.geo-ph] (18 June 2013).
24. E. Bernard, V. Titov, Evolution of tsunami warning systems and products. *Philos. Trans. R. Soc. London Ser. A.* **373**, 20140371 (2015). [doi:10.1098/rsta.2014.0371](https://doi.org/10.1098/rsta.2014.0371) [Medline](#)
25. National Research Council, *Tsunami Warning and Preparedness: An Assessment of the U.S. Tsunami Program and the Nation’s Preparedness Efforts* (National Academies Press, 2011).
26. R. A. Haubrich, W. H. Munk, F. E. Snodgrass, Comparative spectra of microseisms and swell. *Bull. Seismol. Soc. Am.* **53**, 27–37 (1963).
27. V. Titov, A. B. Rabinovich, H. O. Mofjeld, R. E. Thomson, F. I. González, The global reach of the 26 December 2004 Sumatra tsunami. *Science* **309**, 2045–2048 (2005). [doi:10.1126/science.1114576](https://doi.org/10.1126/science.1114576) [Medline](#)

28. M. Simons, S. E. Minson, A. Sladen, F. Ortega, J. Jiang, S. E. Owen, L. Meng, J.-P. Ampuero, S. Wei, R. Chu, D. V. Helmberger, H. Kanamori, E. Hetland, A. W. Moore, F. H. Webb, The 2011 magnitude 9.0 Tohoku-Oki earthquake: Mosaicking the megathrust from seconds to centuries. *Science* **332**, 1421–1425 (2011). [doi:10.1126/science.1206731](https://doi.org/10.1126/science.1206731) [Medline](#)
29. H. Kanamori, L. Rivera, Source inversion of W phase: Speeding up seismic tsunami warning. *Geophys. J. Int.* **175**, 222–238 (2008). [doi:10.1111/j.1365-246X.2008.03887.x](https://doi.org/10.1111/j.1365-246X.2008.03887.x)
30. P. Grangier, R. E. Slusher, B. Yurke, A. LaPorta, Squeezed-light-enhanced polarization interferometer. *Phys. Rev. Lett.* **59**, 2153–2156 (1987). [doi:10.1103/PhysRevLett.59.2153](https://doi.org/10.1103/PhysRevLett.59.2153) [Medline](#)
31. Z. Zhan, Curie Data - Zhan *et al.*, Version 1.0, CaltechDATA (2021); <https://doi.org/10.22002/D1.1668>.
32. A. Galtarossa, L. Palmieri, M. Schiano, T. Tambosso, Measurements of beat length and perturbation length in long single-mode fibers. *Opt. Lett.* **25**, 384–386 (2000). [doi:10.1364/OL.25.000384](https://doi.org/10.1364/OL.25.000384) [Medline](#)
33. J. P. Gordon, H. Kogelnik, PMD fundamentals: Polarization mode dispersion in optical fibers. *Proc. Natl. Acad. Sci. U.S.A.* **97**, 4541–4550 (2000). [doi:10.1073/pnas.97.9.4541](https://doi.org/10.1073/pnas.97.9.4541) [Medline](#)
34. T. H. Chua, C.-L. Chen, Fiber polarimetric stress sensors. *Appl. Opt.* **28**, 3158–3165 (1989). [doi:10.1364/AO.28.003158](https://doi.org/10.1364/AO.28.003158) [Medline](#)
35. R. Ulrich, A. Simon, Polarization optics of twisted single-mode fibers. *Appl. Opt.* **18**, 2241–2251 (1979). [doi:10.1364/AO.18.002241](https://doi.org/10.1364/AO.18.002241) [Medline](#)
36. R. Ulrich, S. C. Rashleigh, W. Eickhoff, Bending-induced birefringence in single-mode fibers. *Opt. Lett.* **5**, 273–275 (1980). [doi:10.1364/OL.5.000273](https://doi.org/10.1364/OL.5.000273) [Medline](#)
37. B. Budiansky, D. C. Drucker, G. S. Kino, J. R. Rice, Pressure sensitivity of a clad optical fiber. *Appl. Opt.* **18**, 4085–4088 (1979). [doi:10.1364/AO.18.004085](https://doi.org/10.1364/AO.18.004085) [Medline](#)
38. J. P. Gordon, “Statistical properties of polarization mode dispersion” in *Polarization Mode Dispersion*, A. Galtarossa, C. R. Menyuk, Eds., vol. 1 of *Optical and Fiber Communications Reports* (Springer, 2004).
39. C. Clivati, A. Tampellini, A. Mura, F. Levi, G. Marra, P. Galea, A. Xuereb, D. Calonico, Optical frequency transfer over submarine fiber links. *Optica* **5**, 893–901 (2018). [doi:10.1364/OPTICA.5.000893](https://doi.org/10.1364/OPTICA.5.000893)
40. C. Clivati, P. Savio, S. Abrate, V. Curri, R. Gaudino, M. Pizzocaro, D. Calonico, Robust optical frequency dissemination with a dual-polarization coherent receiver. *Opt. Express* **28**, 8494–8511 (2020). [doi:10.1364/OE.378602](https://doi.org/10.1364/OE.378602) [Medline](#)
41. G. Charlet, J. Renaudier, H. Mardoyan, P. Tran, O. B. Pardo, F. Verluise, M. Achouche, A. Boutin, F. Blache, J. Y. Dupuy, S. Bigo, Transmission of 16.4-bit/s capacity over 2550 km using PDM QPSK modulation format and coherent receiver. *J. Lightwave Technol.* **27**, 153–157 (2009). [doi:10.1109/JLT.2008.2005506](https://doi.org/10.1109/JLT.2008.2005506)

42. J. C. Geyer, F. N. Hauske, C. R. Fludger, T. Duthel, C. Schulien, M. Kuschnerov, K. Piyawanno, D. van den Borne, E. D. Schmidt, B. Spinnler, H. de Waardt, B. Lankl, B. Schmauss, Channel parameter estimation for polarization diverse coherent receivers. *IEEE Photonics Technol. Lett.* **20**, 776–778 (2008). [doi:10.1109/LPT.2008.921104](https://doi.org/10.1109/LPT.2008.921104)
43. D. E. McNamara, R. I. Boaz, “Seismic noise analysis system using power spectral density probability density functions: A stand-alone software package” USGS Open-File report 2005-1438 (U.S. Geological Survey, 2006).
44. O. Karlsson, J. Brentel, P. A. Andrekson, Long-term measurement of PMD and polarization drift in installed fibers. *J. Lightwave Technol.* **18**, 941–951 (2000). [doi:10.1109/50.850739](https://doi.org/10.1109/50.850739)
45. J. Hansryd, H. Sunnerud, P. A. Andrekson, M. Karlsson, Impact of PMD on four-wave-mixing-induced crosstalk in WDM systems. *IEEE Photonics Technol. Lett.* **12**, 1261–1263 (2000). [doi:10.1109/68.874255](https://doi.org/10.1109/68.874255)
46. M. Karlsson, J. Brentel, Autocorrelation function of the polarization-mode dispersion vector. *Opt. Lett.* **24**, 939–941 (1999). [doi:10.1364/OL.24.000939](https://doi.org/10.1364/OL.24.000939) [Medline](#)
47. M. Shtaif, A. Mecozzi, J. A. Nagel, Mean-square magnitude of all orders of polarization mode dispersion and the relation with the bandwidth of the principal states. *IEEE Photonics Technol. Lett.* **12**, 53–55 (2000). [doi:10.1109/68.817491](https://doi.org/10.1109/68.817491)